

Energy & Environmental Science

Accepted Manuscript



This is an *Accepted Manuscript*, which has been through the Royal Society of Chemistry peer review process and has been accepted for publication.

Accepted Manuscripts are published online shortly after acceptance, before technical editing, formatting and proof reading. Using this free service, authors can make their results available to the community, in citable form, before we publish the edited article. We will replace this *Accepted Manuscript* with the edited and formatted *Advance Article* as soon as it is available.

You can find more information about *Accepted Manuscripts* in the [Information for Authors](#).

Please note that technical editing may introduce minor changes to the text and/or graphics, which may alter content. The journal's standard [Terms & Conditions](#) and the [Ethical guidelines](#) still apply. In no event shall the Royal Society of Chemistry be held responsible for any errors or omissions in this *Accepted Manuscript* or any consequences arising from the use of any information it contains.

ARTICLE

Back-illuminated Si photocathode: a combined experimental and theoretical study for photocatalytic hydrogen evolution

Cite this: DOI: 10.1039/x0xx00000x

Received 00th January 2014,
Accepted 00th January 2014

DOI: 10.1039/x0xx00000x

www.rsc.org/

Dowon Bae,^a Thomas Pedersen,^b Brian Seger,^a Mauro Malizia,^a Andrej Kuznetsov,^c Ole Hansen,^b Ib Chorkendorff,^a Peter C. K. Vesborg^{a†}

Si is an excellent absorber material for use in 2-photon photoelectrochemical hydrogen production. So far nearly all studies of silicon photoelectrodes have employed frontal illumination despite the fact that in most water-splitting 2-photon device concepts the silicon is the “bottom” cell in the tandem stack and therefore illuminated from the back with respect to the electrolyte. In the present work, we investigate back-illuminated Si photoelectrodes experimentally, as well as by modelling, the dependence of induced photocurrent on various parameters, such as carrier diffusion length (L_e) and surface recombination velocity (v_s) to quantify their relative importance. A bifacial light absorbing structure (p⁺pn⁺ Si) is tested under back-illumination conditions which mimic the actual working environment in a tandem water splitting device. The thickness of the absorbing Si layer is varied from 30 to 350 μm to assess the impact of the diffusion length/thickness ratio (L_e/L) on photocatalytic performance. It is shown how the induced photocurrent (J_L) of a back-illuminated sample increases as wafer thickness decreases. Compared to the 350 μm thick sample, a thinned 50 μm thick sample shows a 2.7-fold increase in J_L , and consequently also a higher open circuit voltage. An analytical model is developed to quantify how the relative L_e/L -ratio affects the maximum J_L under back-illumination, and the result agrees well with experimental results. J_L increases with the L_e/L -ratio only up to a certain point, beyond which the surface recombination velocity becomes the dominant loss mechanism. This implies that further efforts should be focused on reduction of surface recombination. The present study is the first experimental demonstration of a Si wafer based photocathode under back-illumination. Moreover, the comparative experimental and theoretical treatment also highlights which photoabsorber properties merit the most attention in the further development towards full tandem water splitting devices.

1. Introduction

The development of semiconductor photocatalytic water splitting devices has attracted recent interest¹⁻⁵ because the direct conversion of solar energy into hydrogen is an attractive route to produce a clean chemical fuel^{2,6,7}.

In order to be competitive with fossil fuels, artificial photosynthesis must be efficient and cheap. The overall process consists of two parts: i) light absorption resulting in charge carrier generation and ii) the utilization of excited photo carriers to drive catalytic reactions at the surface. It is thus essential to harvest a large fraction of the solar spectrum while ensuring efficient charge separation. Dual-absorber systems (sometimes called Z-scheme⁸), represent an efficient way to achieve wide spectral coverage using two semiconductors of different band

gaps (E_g) as shown in Figure 1. Effectively, the dual-absorber system works by series-connecting the high bandgap- and low bandgap-cells enabling a higher total voltage at the expense of current density.

In the case where silicon is used as the low-gap absorber (and as a photocathode in a dual-absorber arrangement) the flat-band potential of p-type silicon places severe restrictions on the voltage in an aqueous electrolyte⁹. However, by replacing the semiconductor-liquid junction with a pn⁺-junction at the surface the flat-band limitation is mitigated. Such pn⁺-Si electrodes have shown efficient electron-hole pair separation and increased open circuit voltage along with a higher current density^{3,4,10,11} compared to p-Si electrodes^{9,12}. In our previous work^{10,11} it was found that pn⁺-Si photocathodes with TiO₂ as a protection layer showed an open circuit voltage (V_{oc}) \geq 0.5 V

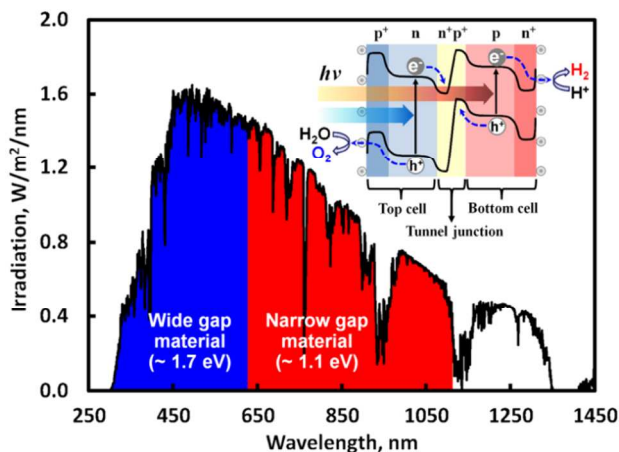


Figure 1. Solar spectrum (AM 1.5G) coverage by dual absorbers based on a Z-scheme, and schematic of a device in a tandem design composed of dual pn-junctions, co-catalysts for oxygen and hydrogen evolution and recombination layer (tunnel junction) (inset). The top cell is formed in a wide band gap material and bottom cell in a narrow band gap material. The inset of this figure illustrates the carrier transfer along the band alignment under incident light. The short wavelength part of the light spectrum is absorbed by the top cell to oxidize water, while the longer wavelengths are absorbed by the bottom cell to produce H_2 gas.

for the Hydrogen Evolution Reaction (HER). These electrodes also showed a maximum photo current (J_L) of 23 mA cm^{-2} under frontal illumination using the red spectrum shown in Figure 1. This non-standard “red light only” illumination serves to simulate a real dual-absorber system where the blue light has been absorbed by the overlying (top) photoelectrode. In that case, 23 mA cm^{-2} corresponds to an Incident Photon to Current Efficiency (IPCE) of nearly 90%, while p-Si photocathodes (without the n^+ layer, but otherwise similar) showed V_{oc} of just 0.05 V with J_L of 17 mA cm^{-2} (IPCE of 61%)⁹.

To date, various dual absorber water splitting devices have been demonstrated experimentally such as pn-GaInP₂/pn-GaAs¹³, pnp-GaInP₂/pn-GaAs¹⁴. These high-efficiency devices, however, are currently too expensive for large-scale applications. It seems that these materials also have severe scalability issues because Ga and In are elements which are by-products (of aluminum and zinc, respectively) and ultimately price-inelastic¹⁵. Various approaches have been demonstrated to substitute these high-cost materials with earth-abundant materials. A Si photocathode coupled to a metal oxide photoanode is one example^{16,17,18}. However, the modest photo current density level of such structures ($J_{L, \text{max}} \approx 0.4 \text{ mA cm}^{-2}$)¹⁷ result in a low efficiency for water splitting. Nevertheless, progress is being made using oxides of lower band gap. A respectable state-of-the-art 3.6% solar-to-hydrogen (STH) efficiency tandem water splitting device based on a doped BiVO₄ photoanode in combination with single junction a-Si solar cell was recently demonstrated¹⁹. Despite recent progress^{3,20}, developing a relatively simple dual absorber tandem structure is still an unsolved engineering challenge.

Using silicon as the bottom cell (*i.e.* under back-illumination – where light is incident from the “dry” side of the

photoelectrode), a series of experiments showed that the photocurrent of a Si bottom cell was limited. The reason is that under back-illumination the electrode-electrolyte interface, which is the electron drain, is on the opposite side with respect to the incident light and since the wafer thickness is larger than the carrier diffusion length most electrons are lost to recombination near the back surface.^{21,22} This problem of opposed light absorption and electrochemistry under back-illumination thus dictates a different approach to maximize the charge carrier utilization.

In this work we evaluate the experimental and theoretical maximum photocurrent ($J_{L, \text{max}}$) limit from the Si based photoelectrochemistry (PEC) system for hydrogen production under the back side illumination. The main focus is on maximum charge utilization of the Si photocathode under the assumption that it is used as a bottom cell in a tandem water splitting device. First we conducted experiments by using Czochralski (CZ) Si based cells with a pn-junction at the electrode/electrolyte interface side (type I configuration²³, see Figure S1a in SI†), but varying the thickness to quantify the effect of the L_e/L -ratio on current-voltage (J-V) performance. We employed a light-permeable Al/p⁺ charge collection backside layer, which allows illumination from the side opposing the solid/liquid interface while mimicking series resistance. A “buried junction” design (type II configuration²³, see Figure S1b in SI†), whose pn⁺-junction is on the illuminated side, can collect charge more efficiently. But the buried junction design requires a very highly doped layer (p⁺) near the electrode-electrolyte interface to form an ultrathin space-charge region which allows electron tunnelling through the interface from the n-type bulk silicon to the electrocatalyst. Without such a layer the charge separation becomes very inefficient²⁴. A key benefit of the type I structure is its ability to reduce the recombination loss of charge carriers by moving the pn-junction to opposite side with respect to the incident light since the presence of dopants increase local bulk recombination which can lead to reduced voltage loss^{25,26}. Many state-of-art photovoltaic (PV) devices employ the same principle to enhance the blue-light response of the cells^{26,27}. In addition, a shallow doped pn⁺-junction formed at electrode-electrolyte interface provides band bending in the silicon independent of the electrolyte. On the other hand - moving the pn junction to the shadow-side of the device requires excellent surface passivation of the light incident side, as we shall see. Most devices in the literature are of a type I configuration, whereas a type II configuration has been demonstrated successfully by using multi-junction III-V^{13,14} and by using a-Si PV devices¹⁹. In addition, we discuss a simplified model of the Si-based cell with the same cross-sectional structure as the aforementioned cell for the experiments to guide the choice of substrate properties: Surface recombination velocity (v_s), diffusion length (L_e) and thickness (L); for HER at maximum current density. The theoretical charge generation and collection models for the analytical calculation are discussed for this case, and finally, we compared the experimental results with the model-based calculation results verify the validity of the model.

2. Methods

2.1. Sample fabrication

CZ-Si based photocathodes of type I are fabricated with different wafer thickness in order to vary the L_e/L ratio ($L = 30 \sim 350 \mu\text{m}$) on otherwise similar electrodes. The thickness of the Si was varied by sample thinning (using photolithography and wet etching) of p-type Si substrates. Schematic drawings of samples used in this work are shown in Figure 2 and Figure S2a in SI†. The shallow pn^+ -junction was produced in p-type (100) Si wafers (Topsil, 1-20 ohm-cm, boron-doped, acceptor density $N_A \approx 5 \cdot 10^{19} \text{ cm}^{-3}$) by thin n^+ doping using phosphorous ion implantation at 36 keV with a dose of $3 \times 10^{15} \text{ cm}^{-2}$ (donor density N_D of approximately $1 \cdot 10^{20} \text{ cm}^{-3}$), which is expected to form a depletion width of 640 nm (described in detail in SI†). As shown in our previous work¹⁰, this n^+ doping screens the band-bending in the silicon from the electrolyte, which allows for increased photovoltage³. As shown in Figure 2c, the electron-hole pairs are separated by a built-in electric field which the pn^+ junction provides. The electrons are then transferred to the solid/liquid interface through the conduction band of TiO_2 using Mott-Shottky analysis (detail calculations are shown in SI†). A mesa-isolated pn^+ -Si structure with height of $3 \mu\text{m}$ is formed at the front side by photolithography and dry etching (Here, we used SF_6 , O_2 and C_4F_8 gases in a Pegasus DRIE system from SPTS Technologies). The back side of the same samples were also doped with a thin p^+ doping using ion implantation of boron at 100 keV with a dose of $5 \times 10^{16} \text{ cm}^{-2}$ ($N_A \approx 1 \cdot 10^{20} \text{ cm}^{-3}$). A metallic charge collecting layer was deposited at room temperature by e-beam evaporation of Al. The Al layer was masked to create a circular hole over the active area in order to allow light transmission to the silicon. The resulting active area was precisely measured by image analysis using ImageJ 1.46r after the experiments. The p^+ doped layer in this device reduces overall series resistance by

providing parallel path ways for holes to reach the Al charge collecting layer. Furthermore in actual tandem device operation condition it can also act as a part of the recombination layer (tunnel junction) for the injected holes from photocathode and the electrons from photoanode. Consequentially, the sample can be stated as a ‘ready-made bottom cell’ for tandem water splitting devices. Samples prepared without the p^+ sheet-conducting layer (Figure S5 in SI†). In order to prevent the Si surface from photo-corrosion during the photo-electrochemical measurements, a Ti/ TiO_2 (5/100 nm) protection layer was sputtered on the n^+ doped side (electrolyte side) of samples using previously published methods^{10,25}. In case of TiO_2 , Ti was reactively sputtered in an oxygen background. Prior to sputter deposition all wafers were dipped in buffered HF for 30 sec, rinsed in Millipore water, dried and were then immediately placed in the sputter chamber to prevent the Si surface from deactivation by native oxide formation. All samples were cleaned with ‘piranha’ solution (3:1 H_2SO_4 (96%): H_2O_2 (30%)), washed with ultrapure water (18 $\text{M}\Omega \text{ cm}$) and dried before having 250 ng (Pt basis) of a dinitrosulphatoplatinate solution (Johnson Matthey) drop-cast on them. Pt was used as a co-catalyst in order to achieve high catalytic activity for HER. The thickness of the wafers was controlled using photolithographically thinned p-type Si substrates to keep the L_e value the same for all samples. Finally, they were coated with Teflon tape with a hole punched out yielding an active area of approximately 0.2 cm^2 . This number was also precisely measured by optical image analysis after the experiments. In addition, the back side of the samples was covered with $50 \mu\text{m}$ thick quartz glass to protect back side from direct contact with the electrolyte. The quartz glass was mounted directly onto the Al layer using epoxy.

2.2. Characterization

A 1000 W Xenon lamp (Oriel) was used with a 635 nm cut-off filter and an AM1.5 filter to simulate the red part of the solar spectrum. The light intensity reaching the sample was measured via a spectrophotometer (International Light Technologies Inc, RPS 900-R), and the light intensity was adjusted to match that of the total light intensity of red light in the AM 1.5G solar spectrum ($\lambda > 635 \text{ nm}$, 41.8 mW cm^{-2}). For electrochemical measurements a Bio-Logic VSP potentiostat was used using EC Lab software. All cyclic voltammetry (CV) experiments were done in a 3 electrode H-cell design with an aqueous 1M HClO_4 (Aldrich 99.99%) electrolyte. For all CV's the electrodes were scanned at a sweep rate of 10 mV sec^{-1} . A Pt mesh was used as a counter electrode and the reference was a saturated Hg/HgSO_4 electrode (VWR International). The solution was purged with H_2 gas 30 minutes prior to any experiment and during the entire duration of the experiment. To determine efficiency as a function of wavelength, incident photon to current efficiency (IPCE) measurements were employed. An Oriel 74100 monochromator was combined with the Xenon lamp mentioned above to give monochromatic light. IPCE measurements were

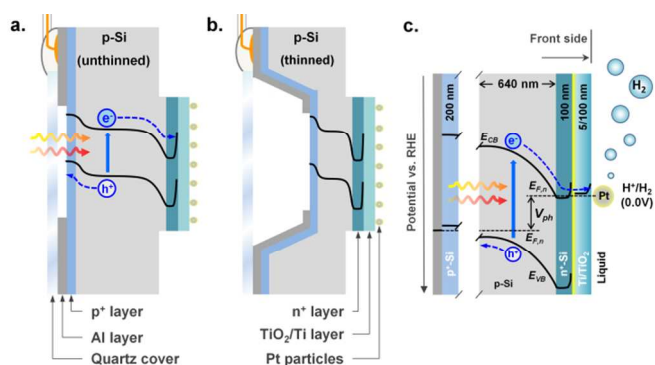


Figure 2. Schematic cross section of the unthinned (a) and thinned device (b) used for photocatalytic activity (HER) experiments. The light is incident from the back side and HER occurs on the front side. In real device testing the back side of sample was protected by Quartz glass cover with epoxy to prevent corrosion in acidic electrolyte of the Cu-wire for electrical connection (covered with glue). Schematic energy diagram (c) of the illuminated sample in equilibrium with H^+/H_2 reaction is also shown. Detail calculation of energy diagram can be found in SI† (also in Figure S3)

carried out from 500 to 900 nm for a thinned sample with a thickness of 50 μm under both front side and back side illumination. Wavelengths below 500 nm are irrelevant in this (bottom cell) study and excluded using a filter. In order to determine the photocurrent, the electrodes were tested at 0.0 V vs. RHE using the same set-up and conditions as the CV measurements. The evolved H_2 was detected by gas chromatography (GC; Hewlett Packard 5890 Series II with a thermal conductivity detector, Ar carrier gas), and this is described in detail in SI†.

2.3. Analytical model calculation

The generation rate is the number of electron-hole pairs generated at each point in the device due to the absorption of photons^{29,30}. Neglecting reflection, the amount of incident light which is absorbed by a material depends on the absorption coefficient $\alpha = \alpha(\lambda)$ (unit cm^{-1}) and the thickness of the absorber. Assuming that the absorption of photons directly causes the generation of an electron-hole pair, the spectral generation rate, G , in a thin slice of absorber is determined by finding the change in light intensity across this thin slice, and consequently the electron-hole generation rate at any point in the device can be defined as follows:

$$G = \alpha H_0 e^{-\alpha z} \quad (1)$$

where H_0 is spectral photon flux density at the surface (photons/sec/unit-area/wavelength increment), and z is distance into the absorber. The overall amount of generated charge at a certain depth is described in theoretical study section (section 3.2). The spectral photon flux density H_0 can be calculated from measured irradiance $P(\lambda)$ of the solar simulator as the ratio of irradiance to photon energy using the equation shown below:

$$H_0 = \frac{\lambda P(\lambda)}{hc} \quad (2)$$

where λ is wavelength, c is the speed of light in vacuum, and h is Planck's constant. In the case where the surface is not perfectly non-reflecting, the irradiance is corrected by measured reflectivity at each wavelength (Figure S8 in SI†). The charge collection probability as a function of depth, $C_P(z)$, was calculated under the assumption that there is no excess electron density at the junction boundary (*i.e.* $n_e = 0$) while at $z = 0$ the surface recombination velocity requires $dn_e/dz = S n_e$, where $S = v_s/D$ is the normalized surface recombination velocity, and v_s is the surface recombination velocity and D is diffusivity of Si. The excess electron density in steady state is governed by the steady state continuity equation:

$$\frac{d^2 n_e}{dz^2} = \frac{n_e}{L_e^2} \quad (3)$$

where $L_e = (D\tau_e)^{1/2}$ is the minority carrier diffusion length, and τ_e is carrier lifetime. The collection probability $C_P(z)$ is the probability that an electron-hole pair generated at a certain depth, z , will be collected (separated) by the pn -junction and consequently contribute to the photocurrent. The behavior of $C_P(z)$ and accompanying photo generated current densities J_L

will be discussed later in theoretical study section, and details of the mathematical derivation can be found in the SI†.

3. Results and discussion

3.1. Experimental study

Since we wish to illuminate from the back, a shallow boron doped p^+ layer, which is formed between the Al back current collector and the p-Si substrate, is used as a hole transport layer. The (control) sample without p^+ doped layer has a very low J_L at 0 V vs. RHE due to a high series resistance (Figure S6 in SI†). Furthermore, this p^+ doped layer works as a part of tunnel junction in practical tandem device. This structure makes the overall series resistance of the device comparable to a conventional Si device with direct back contact, and it was estimated that a doping concentration of 10^{20} cm^{-3} ($5 \cdot 10^{16} \text{ at/cm}^2$ implanted at 100 keV) of boron could provide a sufficiently low sheet resistance to the Si surface³¹, and consequently an efficient carrier transport pathway. Thus, a boron doped p^+ transport layer made by ion implantation method was used in the rest of samples in this study (device structure: $p^+pn^+-\text{Si}$). The photoelectrochemical properties of the $p^+pn^+-\text{Si}$ photocathodes with different thicknesses ($L = 350, 50$ and $30 \mu\text{m}$) were compared by measuring cyclic voltammetry. H_2 could be visually observed bubbling off from the semiconductor/liquid interface as the current increased, and it was confirmed by GC measurement that hydrogen is produced

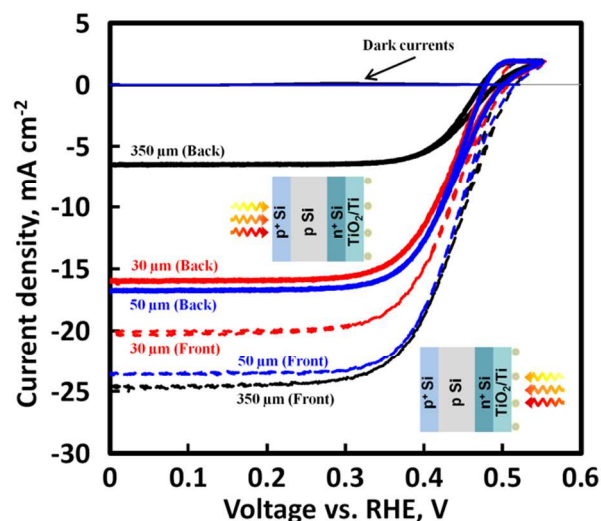


Figure 3. CVs of Si photocathodes with unthinned design (black solid), b with 50 μm thick active area (blue solid) and 30 μm thick active area (red solid) under back-illumination, and under front-illumination (dotted lines). The total irradiance is 41.8 mW cm^{-2} (the light spectrum used in this figure can be found in figure 6). Assuming that L_e of all samples is same, this shows how L_e/L affects J_L of the device. The comparative study between back and front illumination indicates that the thinner the Si absorber is, the larger the ratio of J_L under back and front illumination is. However the $J_{L, \text{max}}$ of 30 μm thick sample with thinned design (red solid) is outperformed by the 50 μm thick sample indicating that absorption losses start to dominate the charge collection losses at around 50 μm thickness.

with high Faradaic efficiency (Figure S9 in SI†). As shown in Figure 3 the fill-factor and photocurrent of 350 μm thick $\text{p}^+\text{pn}^+\text{-Si}$ under front illumination (black dot) was considerably enhanced compared to that of the $\text{pn}^+\text{-Si}$ in Figure S6. This demonstrates that adding the p^+ transport layer between the Al charge collector and p-Si significantly reduces the series resistance of the device. Under back-illumination the 350 μm thick $\text{p}^+\text{pn}^+\text{-Si}$ sample showed a J_L of 6.2 mA cm^{-2} . This is significantly less current than the same sample generates under front-illumination. With the thinned design (Figure 2b) a 50 μm Si slab increased the J_L to 17 mA cm^{-2} under back-illumination at the same light intensity. Since the only change between these samples is thickness, L , this can be considered a result of L_e/L ratio on overall charge to current conversion efficiency. As the b sample was thinned from its back side from 350 to 50 μm the L_e/L ratio should be seven fold larger. Since the diffusion length is the average distance that the excess carriers can cover before they recombine, increased L_e/L ratio should lead to improved J_L . Furthermore, V_{oc} of the thinned $\text{p}^+\text{pn}^+\text{-Si}$ samples shifted slightly cathodic with increased J_L , and their slope improved under the back side illumination. This is likely due to the increased concentration of excited charge carriers. Indeed, the light induced open circuit voltage is given by the equation:

$$V_{oc} = \frac{nkT}{q} \ln \left(\frac{J_L}{J_0} + 1 \right) \quad (4)$$

where n is ideality factor of device, T is operating temperature, k is Boltzmann's constant, q is the electronic charge and J_0 is dark saturation current. Under the assumption that all samples have similar dark current and ideality factor, increased J_L leads to higher V_{oc} . In contrast, comparing unthinned sample with the thinned design (Figure 2b) under front-illumination shows that thinning results in a lower J_L . The reason is that charge generation on average occurs closer to the pn-junction under front-illumination. As a result of the lower photocurrent density the V_{oc} is slightly lower under back-illumination than under front-illumination. This is probably due to a higher effective recombination velocity at the highly doped p^+ side than at the pn^+ -side of the device³². Note also that the 30 μm thick Si

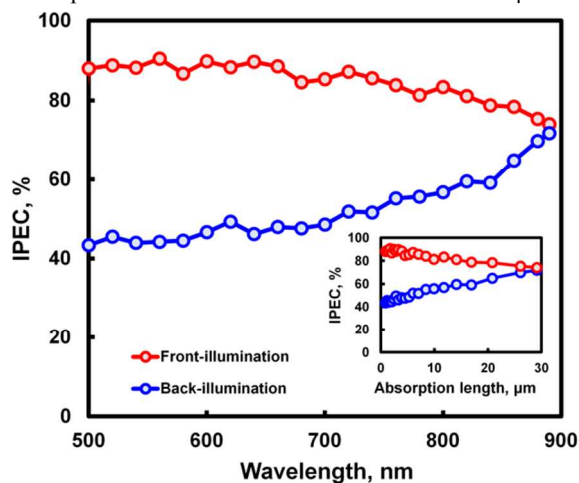


Figure 4. IPCE measurement results under front and back-illumination using 50 μm thick thinned Si sample, and the inset is IPCE curve versus light absorption length (data is shown in Fig S9 in SI†) in Si.

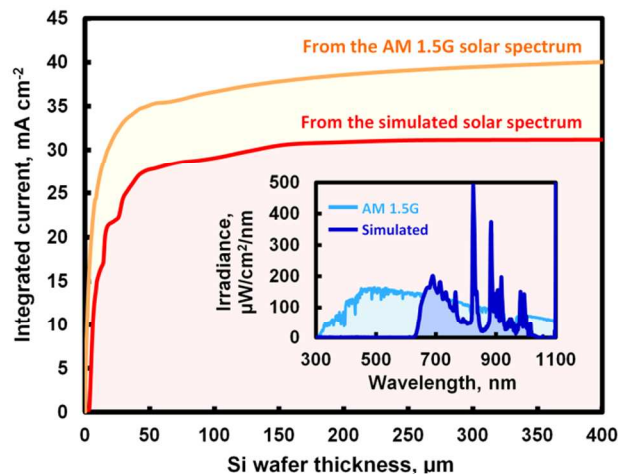


Figure 5. Theoretical light-induced maximum current density in term of Si wafer thickness and the light spectrum of AM 1.5G and solar simulator with AM 1.5 and 635-nm-cut-off filters as an inset. The total irradiance of the simulated solar spectrum is 41.8 mW cm^{-2} , and for the standard AM 1.5G spectrum – 85.1 mW cm^{-2} with range from 250 to 1100 nm in wavelength.

sample with thinned design showed slightly lower current density (16.5 mA cm^{-2}) under back-illumination compared to the otherwise similar 50 μm thick sample even though it has a higher L_e/L ratio. This indicates a thickness of 30 μm is already below the critical thickness where the J_L starts to decrease (*i.e.* loss of photon absorption outweighs gain in $C_p(z)$).

Our spectrally resolved IPCE measurement results agree with this explanation. As shown in Figure 4, the IPCE of a sample with thinned design increases gradually with wavelength under back-illumination, whereas it decreases gradually under the front-illumination. The absorption length δ_p is the distance into a material at which the light intensity drops by a factor of $1/e$ of its original intensity (*i.e.* the effective light penetration depth). Converting wavelength to δ_p in Si allows experimental estimation of $C_p(z)$ under the assumption of similar charge transfer and diffusion efficiency. As shown in the inset of Figure 4, the IPCE was over 90% under front-illumination for photons, which are absorbed near the front side of the sample. Conversely, the same sample showed only approximately 50% IPCE under back-illumination. This shows that the pn^+ -junction region separates charges better than the p^+p -region. The IPCE under back-illumination increases slowly from the short wavelength region and reaches a maximum at a wavelength near 900 nm. This behavior can be explained as follows: Photons with longer wavelengths penetrate deeper into the silicon. So under back-illumination electron-hole pairs generated from longer wavelength photons are therefore generated closer to the pn^+ -junction boundary, whereas front illuminated case the photoabsorption depth as a function of wavelength is inverted, thus the IPCE shows the opposite behavior. This also can be supported by decrease of IPCE of thick samples under back illumination while IPCE under illumination from front side was almost invariable (Fig S9 in SI†).

Since the sample used for this IPCE measurement has a 50 μm thick Si slab, the IPCE response under both back and front illumination almost converge for wavelengths close to 900 nm.

3.2. Theoretical study

3.2.1. Ideal current density vs. effective thickness

Crystalline silicon has an indirect band gap (1.12 eV) and must therefore be thicker than most direct band gap light absorbers in order to have substantial optical absorption and electron-hole pair generation³³. Figure 5 shows, as an inset, the available photons versus wavelength in the reference solar spectrum (AM 1.5G)³⁴. The figure also shows the (red filtered) simulated solar spectrum used in this work where a Xe-lamp illumination is filtered using AM 1.5 and 635-nm-cut-off filters (*i.e.* $\lambda > 635$ nm to approximate the wavelengths and intensity would be received in a real tandem device).

The irradiance of solar light can be converted into a photo-generated electron-hole density (mA cm^{-2}) per unit wavelength for a Si-slab device of finite thickness. The resulting (integrated) current density is shown in figure 5 for both the AM 1.5G reference and for our simulated solar spectrum. If Si were to exhibit ideal behaviour of 100% internal quantum efficiency, *i.e.* zero recombination and infinite diffusion length, this electron-hole density ($J_{theo, max}$) would correspond to the measured photocurrent density. In the calculation of $J_{theo, max}$ the surface reflectance has been set to zero. The effect of surface reflectance will be addressed in detail later in this section. The current density due to photons which are absorbed during a single pass through the Si wafer with a certain thickness x can be theoretically calculated as follows:

$$J_{L,x} = \int_{\lambda_{min}}^{\lambda_g} q \frac{\lambda P(\lambda)}{hc} a(\lambda) d\lambda \quad (5)$$

The integration limits are λ_g (the absorption edge of material), and λ_{min} (the shortest wavelength of the light) taken as 1100 nm and 250 nm in this work. The total irradiance of the (red filtered) simulated solar spectrum measured in this range was 41.8 mW cm^{-2} , which corresponds to the total light intensity of the standard AM 1.5G spectrum with range from 635 nm to 1100 nm. $a(\lambda)$ is the absorbance of the Si slab with a certain thickness, and can be approximated by Beer-Lambert law³⁵ (assuming that light only passes once through the cell and all light generated carriers are collected):

$$a(\lambda) = \frac{\alpha(\lambda)}{\ln 10} L \quad (6)$$

where L is Si thickness, and n is the index of refraction of the Si slab. The absorption coefficient $\alpha(\lambda)$ as a function of wavelength used in this work can be found in Figure S7 in SI†.

The absorbed light flux depends on the absorption length of the light in the silicon. As shown in Figure 5, approximately 40 and 31 mA cm^{-2} of current density can be harvested in an ideal Si photo absorber (if the Si is sufficiently thick), from AM 1.5G and (red filtered) simulated solar spectrum respectively. This figure also indicates that the integrated current density begins to saturate at thicknesses around 50 μm Si with a current density level of approximately 35.7 mA cm^{-2} and 27.7 mA cm^{-2} , under AM 1.5G and (red filtered) simulated solar spectrum respectively. This reveals that there is no need for using a thick wafer. In fact, a silicon back-electrode of just 15 - 25 μm thickness would be able to current match a 10 mA cm^{-2} - or even 15 mA cm^{-2} top electrode in a tandem device. However, as

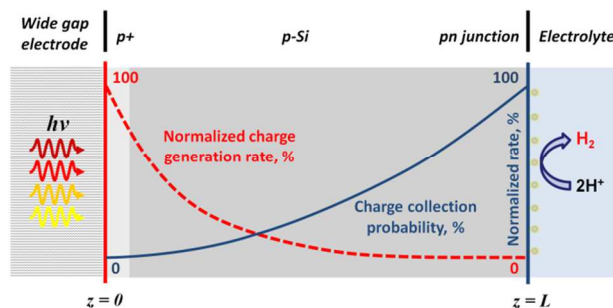


Figure 6. Schematic of the simplified back-illuminated model device which is used in theoretical modelling. The normalized charge generation and charge collection probabilities in the device are also illustrated (not to scale) as a function of depth (z) inside the absorber with thickness L . It was assumed that optical properties of Si are homogeneous regardless of doping type.

we shall see below, introduction of realistic losses recommends a somewhat thicker silicon absorber.

3.2.2. Charge collection model in a real Si device

In real Si devices finite charge recombination and charge diffusion lengths are major limiting factors reducing $J_{L, max}$. It is important to note that neither front nor back surface treatment for light trapping are used in experiments. Therefore we introduce the non-light trapping charge generation rate ($G(z)$), and the charge collection probability ($C_P(z)$) to quantify $J_{L, max}$ in real devices. We have introduced a simplified device model (Figure 6) based on Si with a shallow pn^+ -junction at the electrode-electrolyte interface. Schematic curves of $C_P(z)$ and $G(z)$ are shown in Figure 7 to illustrate the principle. $C_P(z)$ depends on the distance that a light-generated carrier must travel compared to the diffusion length, L_e , and also on the surface properties of the device. If the carrier is generated further away from the junction than a diffusion length, ($z > L_e$), then the collection probability of this carrier is quite low. Similarly, if the carrier is generated closer to a region with high recombination (*e.g.* a non-passivated surface) than the junction, the carrier will recombine. Under, broad-band illumination most of the absorption (and electron-hole generation) takes place very close to the incident light surface (Figure 6). Further absorption of low energy photons takes place throughout the bulk of the silicon, but the excitation density is small. However, the charge collection probability is highest near the pn^+ -junction – *i.e.* the back side with respect to illumination. The dilemma is illustrated in Figure 6.

The rate of light-generated carriers, G , as a function of depth z in Si can be theoretically calculated:

$$G(z) = \int_{\lambda_{min}}^{\lambda_g} \alpha(\lambda) H_0(\lambda) e^{(-\alpha(\lambda)z)} d\lambda \quad (7)$$

Figure 8a shows behavior of $G(z)$ in terms of the depth from the light incident surface. An interesting point from Figure 8a is that $G(z)$ drops below 50% of its initial value (*i.e.* at $z = 0$) just 5 μm from the surface. In fact, charge generation is almost zero at the junction boundary. This underscores the importance of charge collection probability ($C_P(z)$) since only collected charge become external photocurrent. The $C_P(z)$ as a function of depth, z , can be calculated from the equation shown below:

$$C_p(z) = \frac{1}{\cosh \frac{L-z}{L_e} + \sinh \frac{L-z}{L_e} \cdot \frac{\sinh \frac{z}{L_e} + SL_e \cosh \frac{z}{L_e}}{\cosh \frac{z}{L_e} + SL_e \sinh \frac{z}{L_e}}} \quad (8)$$

where S is the normalized surface recombination velocity (surface recombination velocity/diffusivity, $S = v_s/D$) and L , and L_e are the same as their previous definitions. Equation 8 was derived from the ratio of the charge flux at the pn-junction boundary to the sum of the fluxes generated in bulk as described in detail in SI†. As shown in Figure 7b and c, as one moves away from the junction at $z = L$, the collection probability drops. $C_p(z)$ becomes quite low at the surface (at $z = 0$) where electron-hole generation is fastest. The impact of surface recombination velocity and diffusion length on collection probability is also illustrated by varying S (and L_e/L) in Equation 8. As shown in Figure 7b, $C_p(z)$ increases with the L_e/L ratio, and begins to saturate from an approximate ratio of $L_e/L = 2$ with $C_p(z)$ below 20% at the surface. Likewise, $C_p(z)$ increases with decreasing S , but unlike the L_e/L ratio, $C_p(z)$ at the surface ($z = 0$) increases significantly as S value decreases. This indicates that increasing the diffusion length (L_e) increases the charge collection efficiency ($C_p(z)$) only up to a certain point. Beyond this point further increase of diffusion length of the Si (i.e. the bulk quality of the Si) has little benefit for charge collection since in that limit the total recombination is dominated by surface recombination. This behavior of $C_p(z)$, and consequently $J_{L,max}$ for different thicknesses is shown as a function of S and L_e in Figure 8. The $J_{L,max}$ can be calculated from the equation shown below by multiplying $G(z)$ and $C_p(z)$ of the carriers:

$$J_{L,max} = q \int_0^L G(z)C_p(z)dz \quad (9)$$

As shown in each plot of Figure 8, once L_e reaches a certain value comparable to the absorber thickness, surface recombination (S) starts to become more significant. As shown in Figure 8a ($L = 15 \mu\text{m}$), the slopes of contour lines are relatively moderate in the short diffusion length region and the gap between the lines have been broadened. This indicates J_L in a real device will be less sensitive to device parameters, but the maximum current for 15 μm thick Si is limited below 17 mA cm^{-2} while a 30 μm thick Si (Figure 8b) can reach above 20 mA cm^{-2} . The thinnest samples are limited by photons with long wavelength passing through the Si with little absorption. On the other hand, a 350 μm thick device (Figure 8f) shows a J_L limited at approximately 10 mA cm^{-2} and even this value requires good surface passivation and a very high L_e level which only can be achieved by using quality material such as float zone (FZ) Si.

The reason is that charge collection probability with identical S and L_e decreases with increased Si thickness due to the decreased L_e/L ratio and the impact of this ratio increases significantly as thickness of Si increases as already shown in Figure 7c. Clearly, the choice of thickness is strongly dependent on L_e and S and must be optimized with respect to cost. Considering that conventional solar cell grade CZ Si wafer shows L_e of $100 \sim 300 \mu\text{m}$,³⁵ using Si with thickness around 50 μm seems an appropriate compromise. As shown in Figure 8c,

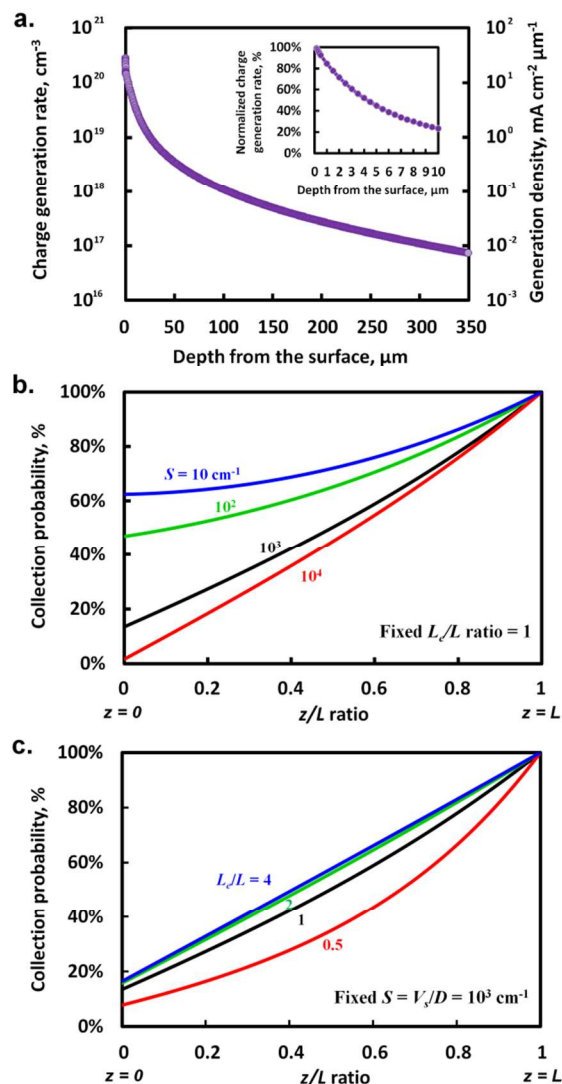


Figure 7. Calculated charge generation induced by the light from the (red) simulated solar spectrum shown in figure 2 (a), calculated collection efficiency with various $S = v_s/D$ (b) and L_e/L (c) ratio. The normalized charge generation rate is ratio of charge generation rate to that at the surface ($z = 0$), where the value shows its maximum.

50 μm thick Si shows peak values up to 22.3 mA cm^{-2} under the $\lambda > 635 \text{ nm}$ simulated spectrum. This is a high J_L value compared to the other thicknesses with identical S and L_e . However, in order to compare to experimental results it is necessary to include the surface reflectance from the light incident side. Considering measured reflectance from the back side of the device (solid blue curve in Figure S11†), the theoretical maximum current with surface reflectance $J_{L,max}$ can be calculated. The result is reduced charge generation rate $G'(z)$ due to the surface reflectance. As shown in Figure 10, it is observed that the overall current level is decreased by more than 15% for all three thicknesses due to the surface reflectance. Overlapping contour lines, which correspond to the experimental values with uncertainty, allows estimating approximate L_e and S values of the Si device used in this work

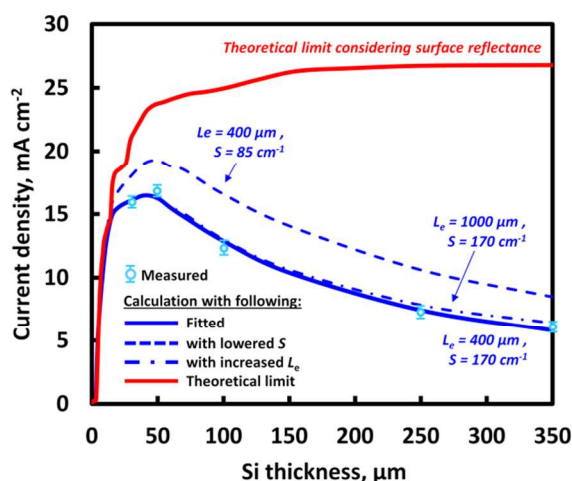


Figure 10. Calculated theoretical limits of the current density: curve from the Si device with recombination rate and diffusion length value traced from the IPCE and modelling data ($L_e = 175 \mu\text{m}$; $S = 0.48 \text{ cm}^{-1}$) (blue solid), and estimated behavior from the device with increased L_e and S (blue dots). Theoretical limit of an ideal Si device, i.e. $L_e = \infty$ and $S = 0$ (red curve) with surface reflectance is also given for comparison.

can be an excellent candidate as demonstrated by Panasonic HIT cell²⁶, since a-Si:H has excellent passivation capability and enable good carrier transport. It should be noted that the conduction band position of the n-type TCO layer should be close to the valence band of p^+ Si surface⁴², since these layers should work as a tunnel junction in practical tandem device.

4. Conclusion

We have demonstrated, for the first time, a back-illuminated photocathode which is suited to work efficiently in a tandem PEC stack. Specifically we have shown that a photocathode with a p^+pn^- -Si – structure, whose pn-junction is formed at the solid/liquid side, can be used as a HER photoelectrode under back side (dry side) illumination which is similar to actual operational conditions in tandem water splitting devices. From an analytical calculation study, it was found that the balance between charge collection probability and light absorber thickness is an important design parameter to produce efficient back-illuminated devices. The photoelectrochemical investigation of p^+pn^- -Si with Si-thickness as parameter clearly demonstrates the impact of L_e/L ratio estimated from the abovementioned theoretical results. A 50 μm thick thinned p^+pn^- -Si electrode showed a maximum J_L (17.0 mA cm^{-2}) under back-illumination, whereas a 350 μm thick sample, with a 7 times lower L_e/L ratio, showed only 6.1 mA cm^{-2} . In contrast, despite its enhanced L_e/L ratio, a 30 μm thick sample showed only slightly lower J_L due to its limited light absorption (loss of infrared photons). These results demonstrate how the charge collection limitation of a photocathode with its pn-junction at solid/liquid can be overcome. Importantly, the increased fill factor and increased V_{oc} of the thinned back-illuminated samples owe their success mostly to increased J_L , and such designs should lead to increased operational current density

when coupled with a photoanode. Building on the experimental input, further modelling shows that surface recombination on the back side of the silicon is the dominant current loss mechanism. Therefore, the application of a conducting passivation layer, which allows transport of the carriers with minimum optical loss, seems one of the critical challenges to reduce the back side recombination rate and consequently enhance photocatalytic performance of practical Si-bottom cell.

Acknowledgements

This work was performed as a part of the Center for Individual Nanoparticle Functionality (CINF) which is funded by Danish National Research Foundation (DNRF54). Furthermore, most of sample fabrication work has been done using facilities in DTU Danchip.

Notes and references

^aCenter for Individual Nanoparticle Functionality, Department of Physics, Technical University of Denmark, 2800 Kgs. Lyngby, Denmark

[†]Peter.Vesborg@fysik.dtu.dk; Fax: +45 4593 2399; Tel: +45 4525 3276

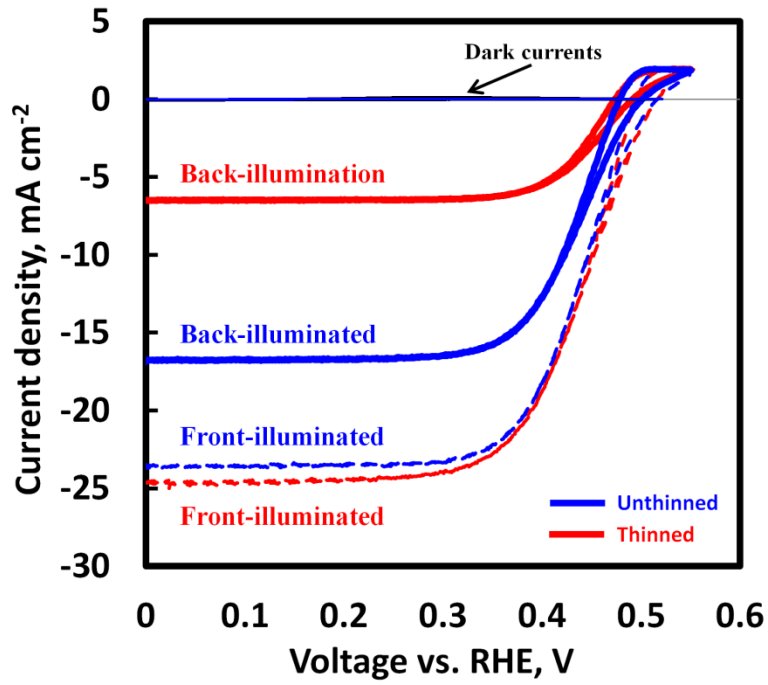
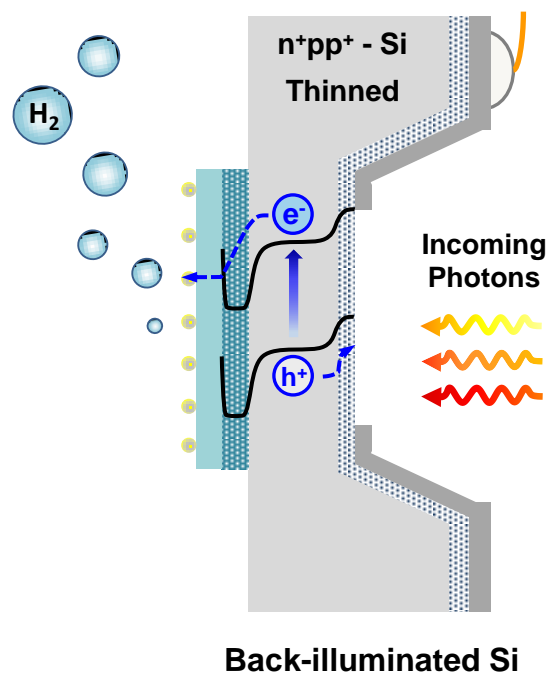
^bDepartment of Micro- and Nanotechnology, Technical University of Denmark, 2800 Kgs. Lyngby, Denmark.

^cCentre for Materials Science and Nanotechnology, Department of Physics, University of Oslo, 0316 Oslo, Norway.

† Electronic Supplementary Information (ESI) available: Supplementary information accompanies this paper including supplementary figures S1-8; mathematical derivation procedure for analytical modelling; detail sample fabrication and equipment information for the experiments.

1. N. S. Lewis and D. G. Nocera, *Powering the planet: chemical challenges in solar energy utilization*, Proc. Natl. Acad. Sci. U. S. A., 2006, **103**, 15729–15735.
2. M. G. Walter, E. L. Warren, J. R. McKone, S. W. Boettcher, Q. Mi, E. A. Santori, N. S. Lewis, *Solar water splitting cells*, Chem. Rev., 2010, **110**, 6446–6473.
3. S.W. Boettcher, E. L. Warren, M. C. Putnam, E. A. Santori, D. Turner-Evans, M. D. Kelzenberg, M. G. Walter, J. R. McKone, B. S. Brunschwig, H. A. Atwater, N. S. Lewis, *Photoelectrochemical hydrogen evolution using Si microwire Arrays*, J. Am. Chem. Soc., 2011, **133**, 1216–1219.
4. M. Moriya, T. Minegishi, H. Kumagai, M. Katayama, J. Kubota, K. Domen, *Stable hydrogen evolution from CdS-modified CuGaSe₂ photoelectrode under visible-light irradiation*, J. Am. Chem. Soc., 2013, **135**, 3733–3735.
5. C. G. Morales-Guio, S. D. Tilley, H. Vrubel, M. Grätzel, X. Hu, *Hydrogen evolution from a copper(I) oxide photocathode coated with an amorphous molybdenum sulphide catalyst*, Nat. Commun., 2014, **5**, 3059.
6. S. Dahl, I. Chorkendorff, *Solar-fuel generation: becoming practical?*, Nat. Mater., 2012, **11**, 100–101.
7. R. Schlögl, *Chemistry's role in regenerative energy*, Angew. Chem. Int. Ed. 2011, **50**, 6424–6426.
8. A. J. Bard, *Photoelectrochemistry and heterogeneous photo-catalysis at semiconductors*, J. Photochem., 1979, **10**, 59 – 75.

9. Y. Hou, B. L. Abrams, P. C. K. Vesborg, M. E. Björketun, K. Herbst, L. Bech, A. M. Setti, C. D. Damsgaard, T. Pedersen, O. Hansen, J. Rossmeis, S. Dahl, J. K. Nørskov, I. Chorkendorff, *Bioinspired catalysts bonded to a Silicon photocathode for solar Hydrogen evolution*, *Nat. Mater.*, 2011, **10**, 434-438.
10. B. Seger, T. Pedersen, A. B. Laursen, P. C. K. Vesborg, O. Hansen, I. Chorkendorff, *Using TiO₂ as a conductive protective layer for photocathodic H₂ evolution*, *J. Am. Chem. Soc.*, 2013, **135**, 1057-1064.
11. B. Seger, A. B. Laursen, P. C. K. Vesborg, T. Pedersen, O. Hansen, S. Dahl, I. Chorkendorff, *Hydrogen production using a molybdenum sulfide catalyst on a titanium-protected n+p-silicon photocathode*, *Angew. Chem. Int. Ed.*, 2012, **51**, 9128-9131.
12. E. L. Warren, S. W. Boettcher, J. R. McKone, N. S. Lewis, *Photoelectrochemical water splitting: silicon photocathodes for hydrogen evolution*, *Proc. of SPIE*, 2010, **7770**, 77701F-1.
13. B. O. Khashelev, J. A. Turner, *A monolithic photovoltaic-photoelectrochemical device for hydrogen production via water splitting*, *Science*, 1998, **280**, 425-427.
14. X. Gao, S. Kocha, A. J. Frank, J. A. Turner, *Photoelectrochemical decomposition of water using modified monolithic tandem cells*, *Int. J. Hydrogen Energ.*, 1999, **24**, 319-325.
15. P. C. K. Vesborg, T. F. Jaramillo, *Addressing the terawatt challenge: scalability in the supply of chemical elements for renewable energy*, *RSC Adv.*, 2012, **2**, 7933-7947.
16. R. H. Coridan, M. Shaner, C. Wiggenshorn, B. S. Brunshwig, N. S. Lewis, *Electrical and photoelectrochemical properties of WO₃/Si tandem photoelectrodes*, *Phys. Chem. C.*, 2013, **117**, 6949-6957.
17. M. R. Shaner, K. T. Fountaine, S. Ardo, R. H. Coridan, H. A. Atwater, N. S. Lewis, *Photoelectrochemistry of core-shell tandem junction n-p⁺-Si/WO₃ microwire array photoelectrodes*, *Energ. Environ. Sci.*, 2014, **7**, 779-790.
18. J. A. Turner, *A nickel finish protects silicon photoanodes for water splitting*, *Science* 2013, **342**, 811-812.
19. F. F. Abdi, L. Han, A. H. M. Smets, M. Zeman, B. Dam, R. van de Krol, *Efficient solar water splitting by enhanced charge separation in a bismuth vanadate-silicon tandem photoelectrode*, *Nat. Commun.*, 2013, **4**, 2195.
20. J. Brilliet, J.-H. Yum, M. Cornuz, T. Hisatomi, R. Solarska, J. Augustynski, M. Graetzel, K. Sivula, *Highly efficient water splitting by a dual-absorber tandem cell*, *Nature Photon.*, 2012, **6**, 824-828.
21. N. Wyrsh, S. Dunand, C. Ballif, *Bifacial a-Si:H solar cells: Origin of the asymmetry between front and back illumination*, *Proceedings of NUMOS*, 2007, 289-295.
22. A. Kränzl, R. Kopecek, K. Peter, P. Fath, *Bifacial solar cells on multi-crystalline silicon with boron BSF and open rear contact*, *Conference Record of the 2006 IEEE 4th World Conference on Photovoltaic Energy Conversion*, 2006, **1**, 968-971.
23. S. Hu, C. Xiang, S. Haussener, A. D. Berger, N. S. Lewis, *An analysis of the optimal band gaps of light absorbers in integrated tandem photoelectrochemical water-splitting systems*, *Energ. Environ. Sci.*, 2013, **6**, 2984-2993.
24. J. J. H. Pijpers, M. T. Winkler, Y. Surendranath, T. Buonassisi, D. G. Nocera, *Light-induced water oxidation at silicon electrodes functionalized with a cobalt oxygen-evolving catalyst*, *Proc Natl Acad Sci U. S. A.* 2011, **25**, 10056-10061.
25. D. L. Meier, H. P. Davis, R. A. Garcia, J. Salami, A. Rohatgi, A. Ebong, P. Doshi, *Aluminum alloy back p-n junction dendritic web silicon solar cell*, *Sol Energ Mat Sol C*, 2001, **65**, 621-627.
26. Panasonic headquarter news, http://panasonic.co.jp/corp/news/official_data/data_dir/2014/04/en140410-4/en140410-4.html, (accessed November 2014).
27. D. D. Smith, P. J. Cousins, A. Masad, A. Waldhauer, S. Westerberg, M. Defensor, R. Ilaw, T. Dennis, R. Daquin, N. Bergstrom, A. Leygo, Z. Xi, B. Meyers, B. Bourne, M. Shields, D. Rose, *SunPower's Maseon Gen III solar cell: High efficiency and energy yield*, *Proc. 39th IEEE PVSC, IEEE*, New York, 2013, 0908-0913.
28. Y. Lin, C. Battaglia, M. Boccard, M. Hettick, Z. Yu, C. Ballif, J. W. Ager, A. Javey, *Amorphous Si thin film based photocathodes with high photovoltage for efficient hydrogen production*, *Nano Lett.*, 2013, **13**, 5615-5618.
29. F. Y. R. El Fauturi, A. Y. Darkwi, *Computer simulation for current density in pn-Si solar cells*, *Proceedings of the International Symposium on Solar Physics and Solar Eclipses*, Waw an Namus, 2006.
30. C. Hu, R. M. White, *Solar Cells: from basics to advanced systems*, ed. W. Stephen, McGraw-Hill college, New York, 1st den., 1983, ch. 3.3, pp. 45-46.
31. W. R. Thurber, R. L. Mattis, Y. M. Liu, J. J. Filliben, *Resistivity-dopant density relationship for boron-doped silicon*, *J. Electrochem. Soc.*, 1980, **127**, 2291-2294.
32. A. F. Thomson, K. R. McIntosh, *Light-enhanced surface passivation of TiO₂-coated silicon*, *Prog. Photovoltaics*, 2012, **20**, 343-349.
33. P. Bosshard, W. Hermann, E. Hung, R. Hunt, A. J. Simon, *An assessment of solar energy conversion technologies and research opportunities*, GCEP Energy Assessment Analysis, Stanford University, 2006.
34. ASTM G173-03, *Standard tables for reference solar spectral irradiances: direct normal and hemispherical on 37° tilted surface*, 2012.
35. V. A. Milichko, A. I. Nechaev, V. A. Valtsifer, V. N. Strelnikov, Y. N. Kulchin, V. P. Dzyuba, *Photo-induced electric polarizability of Fe₃O₄ nanoparticles in weak optical fields*, *Nanoscale Res. Lett.*, 2013, **8**, 317-323.
36. D. L. Losee, *Admittance spectroscopy of impurity levels in Schottky barriers*, *J. Appl. Phys.*, 1975, **46**, 2204-2214.
37. T. W. Kim, K.-S. Choi, *Nanoporous BiVO₄ photoanodes with dual-layer oxygen evolution catalysts for solar water splitting*, *Science*, 2014, **343**, 990-994.
38. F. Feldmann, M. Simon, M. Bivour, C. Reichel, M. Hermlle, and S. W. Glunz, *Carrier-selective contacts for Si solar cells*, *Appl. Phys. Lett.* 2014, **104**, 181105.
39. D. Garcia-Alonso, S. Smit, S. Bordihn, W. M. M Kessel, *Silicon passivation and tunneling contact formation by atomic layer deposited Al₂O₃/ZnO stacks*, *Semicond. Sci. Tech.*, 2013, **28**, 082002.
40. A. Goodrich, P. Hacke, Q. Wang, B. Sopori, R. Margolis, T. L. James, M. Woodhouse, *A wafer-based monocrystalline silicon photovoltaics roadmap: Utilizing known technology improvement opportunities for further reductions in manufacturing costs*, *Sol. Energ. Mat. Sol. C.*, 2013, **114**, 110-135.
41. J. Schmidt, M. Kerr, A. Cuevas, *Surface passivation of silicon solar cells using plasma-enhanced chemical-vapour-deposited SiN films and thin thermal SiO₂/plasma SiN stacks*, *Semicond. Sci. Technol.*, 2001, **16**, 164-170.
42. Y. -S. Lin, S. -Y. Lien, C. -C. Wang, C. -H. Hsu, C. -H. Yang, A. Nautiyal, D. -S. Wu, P. -C. Tsai, S. -J. Lee, *Optimization of recombination layer in the tunnel junction of amorphous silicon thin-film tandem solar cells*, *Int. J. Photoenergy*, 2011, **2011**, 264709.



Back-illuminated Si photocathode: a combined experimental and theoretical study for photocatalytic hydrogen evolution

Dowon Bae,¹ Thomas Pedersen,² Brian Seger,¹ Mauro Malizia,¹ Andrej Kuznetsov,³ Ole Hansen,² Ib Chorkendorff,¹ Peter C.K. Vesborg^{1†}

¹Center for Individual Nanoparticle Functionality, Department of Physics, Technical University of Denmark, 2800 Kgs. Lyngby

²Department of Micro- and Nanotechnology, Technical University of Denmark, 2800 Kgs. Lyngby

³Centre for Materials Science and Nanotechnology, Department of Physics, University of Oslo, 0316 Oslo, Norway

Supplementary Information

1. Energy band diagrams of tandem PV assisted PEC system

A “buried junction” bottom cell design whose pn-junction is formed on the light incoming side can collect charge more efficiently, but the injection of electrons to the electrolyte can be hindered due to the upward band bending at the semiconductor/liquid interface (the bulk is now n-type). A sufficiently highly doped layer is required to minimize the thickness of the upward band bending region at the semiconductor/liquid interface so that injected electrons can tunnel through the interface. On the other hand, type I has an advantage over type II in easy injection of the collected charges by its shallow pn-junction at the semiconductor/liquid interface. And this pn-junction isolates the band-bending to within the photo-absorber. However, one cannot avoid charge collection losses due to the distant position of pn-junction from the light incident surface.

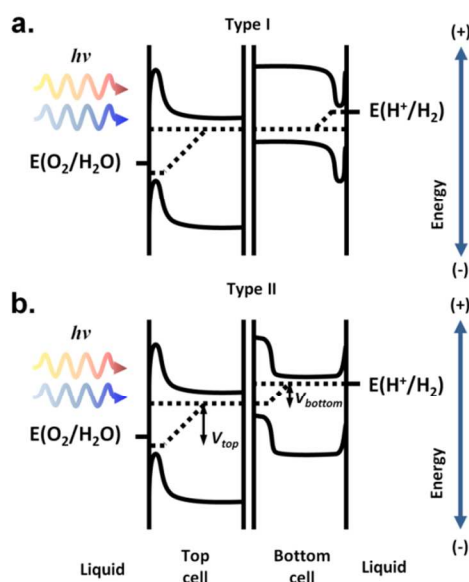


Figure S 1. Schematic energy band diagrams of tandem PV assisted PEC system for the configuration (a) with semiconductor/liquid junction (type I), and (b) the configuration (b) with buried junction (type II).

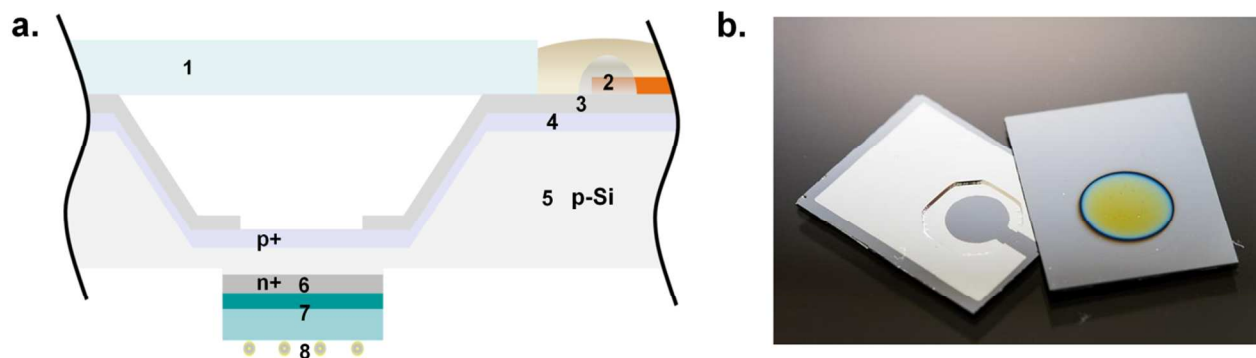


Figure S 2. Schematic cross section of multilayered-structure with classification numbers by its function (a), and optical image of cells used in this work (back-illuminated surface – left, front-illuminated surface – right). These samples were covered with Quartz glass and Teflon tape before the photochemical experiments.

Table S 1. Information of layers classified by its function in Figure S2.

N ^o	Function	Material	Method
1	Cover window	Quartz glass	Epoxy bonding
2	Charge collector	Cu wire	Ag-paste
3	Back contact	Al	E-beam evaporator
4	Charge transfer (p ⁺) layer	Boron-doped Si	Ion-implantation
5	Light absorber (p)	p-type Si	(100) CZ wafer
6	pn-junction (n ⁺ layer)	Phosphorous-doped Si	Ion-implantation
7	Protection layer	TiO ₂ /Ti	DC sputtering with O ₂ flow
8	Co-catalyst	Pt	Drop-casting (10 μL)

2. Structure and sample fabrication methods

A TiO₂/Ti layer was used as a corrosion protection layer at the semiconductor/liquid junction, and Pyrex glass cover as an isolation layer for the back-side to prevent from unexpected reaction. p⁺ and n⁺ doped layer were formed by doping with Boron and Phosphorous, respectively, using ion implantation, which was followed by annealing of the samples using rapid thermal process for distribution of implanted ions with minimized thermal redistribution of impurities at high temperature. The Al charge collecting layer was deposited by using the E-beam evaporation process. A circular hole for light incident in the middle of thinned surface was formed by using metallic shadow mask during the evaporation process. The deposited Al area was turned into a fully connected area using Silver paint to leave a non-Al circular area with a diameter of 5 mm. The areas of these circular holes were measured precisely by using image analysis program

ImageJ 1.46r. The front surfaces (bottom surface in Figure S2a) were covered by hole punched (\varnothing 5 mm) Teflon tape, and these holes were also measured precisely using the image analysis program. The Pt was drop-casted as a last step onto the opened TiO₂ surface. The detailed information of layers classified by its function can be found in Table S1.

3. Calculation for band diagram

3.1. Calculation at pn⁺-junction

Most of this band diagram has already been demonstrated in our previous works¹. In explaining the band diagram, we will start from the pn-junction of electrode and move towards the electrolyte. The p-Si wafer has a band gap (E_g) of 1.124 eV, an acceptor density (N_A) of $3 \cdot 10^{15} \text{ cm}^{-3}$. The bulk p-Si valence band (VB) can be determined as a function of working potential (E):

$$E_{V,p-si} = E - \frac{kT}{e} \ln \left(\frac{N_{A,p-si}}{N_{V,si}} \right)$$

In figure S3 the working potential corresponds to the hole quasi-Fermi level. k is Boltzmann's constant, T is temperature (298 K), e is the elementary charge, and $N_{V,si}$ is the density of states in the valence band, which is $1.8 \cdot 10^{19} \text{ cm}^{-3}$ for Si². Assuming the pinning of the band edges of the semiconductor at the interface (0 V vs. RHE) the $E_{V,p-si}$ is 0.22 V.

The Surface of the p-Si was doped with phosphorous by ion implantation process and n⁺ emitter layer was formed at the surface. The process simulation program (Athena, SILVACO) was used to determine the donor density (N_D), which is approximately $5 \cdot 10^{19} \text{ cm}^{-3}$. The bulk valence band of the n⁺ Si can be determined via equation:

$$E_{C,n-si} = E + \frac{kT}{e} \ln \left(\frac{N_{D,n-si}}{N_{C,si}} \right)$$

where N_C stands for the density of states in the conduction band, which is $2.8 \cdot 10^{19} \text{ cm}^{-3}$ for Si². Under the same assumption as above the $E_{C,n-si}$ is 0.015 V.

At the pn⁺-junction a built-in potential will be formed which can be determined in the dark via equation:

$$V_{bi} = \frac{kT}{e} \ln \left(\frac{N_{D,n-si} \cdot N_{A,p-si}}{n_i^2} \right)$$

where n_i is intrinsic carrier density of Si, which is approximately $1.5 \cdot 10^{10} \text{ cm}^{-3}$ at room temperature, and V_{bi} was found to be 0.9 V. Under illumination V_{bi} at open circuit voltage conditions will simply be the V_{bi} in the dark minus the photo voltage (V_{ph}):

$$V_{bi,OCV} = V_{bi} - V_{ph}$$

If it is assumed that there are no interfacial losses at the pn^+ -junction, the V_{bias} is distributed between the p-Si and n^+ -Si as followed:

$$V_{bi,p-si} = V_{bi,OCV} \frac{N_{D,n-si}}{N_{A,p-si} + N_{D,n-si}}$$

$$V_{bi,n-si} = V_{bi,OCV} \frac{N_{A,p-si}}{N_{A,p-si} + N_{D,n-si}}$$

Using above equations, the $V_{bi,p-si}$ is 0.43 V and $V_{bi,n-si}$ is $1.3 \cdot 10^{-5}$ V. The depletion width can be determined via equation:

$$W = \sqrt{\frac{2\varepsilon_0\varepsilon_{Si}(N_{D,n-si} + N_{A,p-si})V_{bi}}{eN_{D,n-si}N_{A,p-si}}}$$

where ε_0 ($8.8 \cdot 10^{-12} \text{ F/m}$)³ is the permittivity in vacuum, and ε_{Si} is the relative permittivity of Si (11.7)⁴. From the equation mentioned above the sample was determined to have a depletion width of 640 nm. The depletion width is distributed between the p-Si and n^+ -Si as followed:

$$x_p = \frac{N_{D,n-si}}{N_{A,p-si} + N_{D,n-si}} W$$

$$x_n = \frac{N_{A,p-si}}{N_{A,p-si} + N_{D,n-si}} W$$

From the equation above mentioned, most of depletion width will be in p-Si side and only 0.2 nm will be in n^+ -Si layer.

3.2. Calculation at n^+ -Si/Ti interface

In this work we assume the n^+ -Si/Ti interface forms a Schottky barrier with no metal induced gap states or Fermi level pinning. If this is the case, the barrier height $\Phi_{B,Si}$ at the n^+ -Si/Ti

interface is the difference between the Ti work function ($\Phi_{Ti} = 4.33$ V)⁵ and the n⁺-Si ionization energy (Φ_{n^+-Si}) plus the deviation between the flat band potential and the conduction band. Assuming that Φ_{n^+-Si} is close to the electron affinity of Si ($\chi_{Si} = 4.15$ V)⁶ This is shown in equation below:

$$\Phi_{B,Si} = \Phi_{Ti} - \Phi_{Si} + \frac{kT}{e} \ln \left(\frac{N_{C,Si}}{N_{D,n-Si}} \right)$$

$\Phi_{B,Si}$ was found to be 0.15 V. Since Ti is a metallic layer, and has a high carrier density compared to the Si, thus the bias will be distributed entirely over the n⁺ Si region. The band bending distance in the n⁺-Si can be determined by equation:

$$W_{n^+Si/Ti} = \sqrt{\frac{2\varepsilon_{Si}\varepsilon_0\Phi_B}{eN_{D,n-Si}}}$$

The barrier width was found to be approximately 1.4 nm, and electron transfer from the Si to the Ti would most probably have to occur through tunneling.

3.3. Calculation at TiO₂/liquid interface

From the Mott-Schottky analysis the TiO₂ conduction band was determined to be -0.09 V vs. RHE, the donor density was $4.5 \cdot 10^{19}$ cm⁻³, and the flat band potential was -0.07 V vs. RHE. Since the E_{FB, TiO_2} is very close to the work function of Ti, thus it can be assumed this junction will show Ohmic behavior. From our previous works we have seen that TiO₂-Pt system forms an Ohmic contact, thus there shouldn't be a barrier at the interface¹.

The depletion region width of TiO₂ at the interface is given by:

$$W_{TiO_2/liquid} = \sqrt{\frac{2\varepsilon_0\varepsilon_{TiO_2}\Phi_{B,TiO_2}}{eN_{D,TiO_2}}}$$

ε_{TiO_2} is the relative permittivity of TiO₂ (75)⁷, N_{D,TiO_2} is the doping density of TiO₂ obtained from Mott-Shottky analysis ($4.5 \cdot 10^{19}$ cm⁻³). Φ_{B,TiO_2} is the barrier height at TiO₂/liquid interface, and it can be simply calculated by:

$$\Phi_{B,TiO_2} = E_{H^+/H_2} - E_{FB,TiO_2} + \frac{kT}{e} \ln \left(\frac{N_{D,TiO_2}}{N_{C,TiO_2}} \right)$$

where N_{C,TiO_2} is the density of states in the conduction band, which is $6.8 \cdot 10^{20} \text{ cm}^{-3}$ for TiO_2 ⁸. Since we assume that interface forms Fermi level pinning, above-mentioned equation results in Φ_{B,TiO_2} of 0.038 V. Applying this values results in $W_{TiO_2/liquid}$ of 1.02 nm.

3.4. Calculation at p⁺ p-junction

The shallow doped p⁺-Si VB can be determined through the flat band:

$$E_{V,p^+-Si} = E - \frac{kT}{e} \ln \left(\frac{N_{A,p^+-Si}}{N_{V,Si}} \right)$$

Using acceptor density values of p⁺ Si N_{A,p^+-Si} ($1 \cdot 10^{20} \text{ cm}^{-3}$), the valence band of p⁺ layer is 0.04 V. There are no simple expressions predicting the depletion width, but the width is on the order of a Debye length:

$$L_D = \sqrt{\frac{\epsilon_0 \epsilon_{Si} kT}{e^2 N_{A,p-Si}}}$$

Considering all values used above, the depletion width is approximately 75 nm.

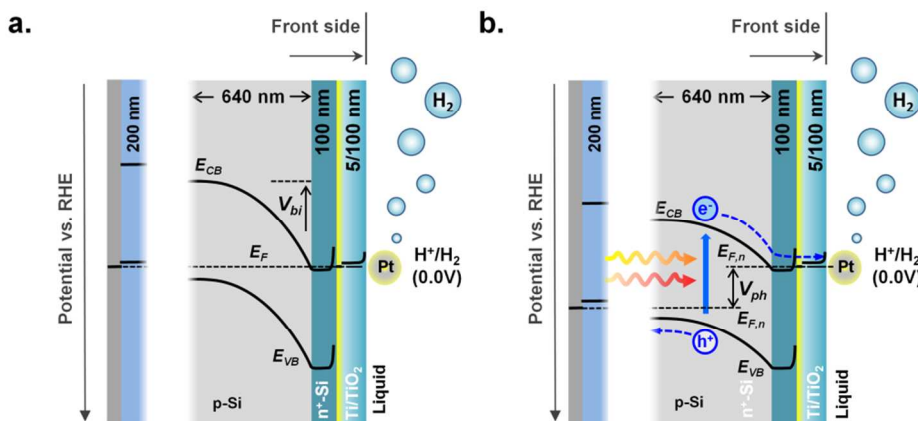


Figure S 3. Schematic energy diagram of the pn⁺ Si with Ti-TiO₂ surface in the dark in equilibrium with the H⁺/H₂ reaction (a), and illuminated condition with photovoltage (b).

Material and device parameters which have been used for the calculation also can be found in table S2:

Table S2. Material and device parameters

Parameter	Definition	Value
$N_{A, p-Si}$	Acceptor density of p-Si	$3 \cdot 10^{15} \text{ cm}^{-3}$ *
$N_{C, Si}$	Density of states of Si in conduction band	$2.8 \cdot 10^{15} \text{ cm}^{-3}$ [2]
$N_{V, Si}$	Density of states of Si in valence band	$1.8 \cdot 10^{19} \text{ cm}^{-3}$ [2]
$N_{D, n-Si}$	Donor density of n ⁺ -Si	$5 \cdot 10^{19} \text{ cm}^{-3}$ **
N_{A, p^+-Si}	Acceptor density of p ⁺ -Si	$1 \cdot 10^{20} \text{ cm}^{-3}$ **
N_{C, TiO_2}	Density of states of TiO ₂ in conduction band	$6.8 \cdot 10^{20} \text{ cm}^{-3}$ [8]
N_{D, TiO_2}	Donor density of TiO ₂	$4.5 \cdot 10^{19} \text{ cm}^{-3}$ ***
χ_{Si}	Electron affinity of Si	4.15 V [3]
Φ_{Ti}	Work function of Ti	4.33 [5]
ϵ_o	Permittivity in vacuum	$8.85 \cdot 10^{-12} \text{ F m}^{-1}$ [3]
ϵ_{Si}	Relative permittivity of Si	11.7 [4]
ϵ_{TiO_2}	Relative permittivity of TiO ₂	75 [7]

*Provided by supplier (Topsil)

**Calculated using a process simulation program (Athena, SILVACO).

***Taken from the experimental Mott-Shottky analysis of TiO₂

4. Mott-Shottky analysis of TiO₂

To determine the TiO₂ conduction band, we provided Mott-Shottky analysis using 100 nm TiO₂/5 nm Ti deposited on n⁺ Si. The n⁺ Si was chosen to prevent unexpected photovoltage effect. This sample was tested electrochemically in 1 M HClO₄ electrolyte. For this experiment a modulation frequency of 10 kHz, perturbation amplitude of 35 mV has been used. Figure S4 shows the result of this experiment.

The flat band potential of TiO₂ can be estimated by using Mott-Shottky equation shown below:

$$\frac{1}{C^2} = \frac{2}{q\epsilon_{TiO_2}\epsilon_o AN_{D,TiO_2}} \left(E - E_{FB} - \frac{kT}{e} \right)$$

where C is the measured differential capacitance per area. Using this equation results in a flat band potential of -0.07 V vs. RHE and dopant density of $4.5 \cdot 10^{19} \text{ cm}^{-3}$.

The conduction band can be found using the equation shown below:

$$E_C = E_{FB} - \frac{kT}{e} \ln \left(\frac{N_{D,TiO_2}}{N_{C,TiO_2}} \right)$$

The equation results in a conduction band at -0.09 V vs. RHE.

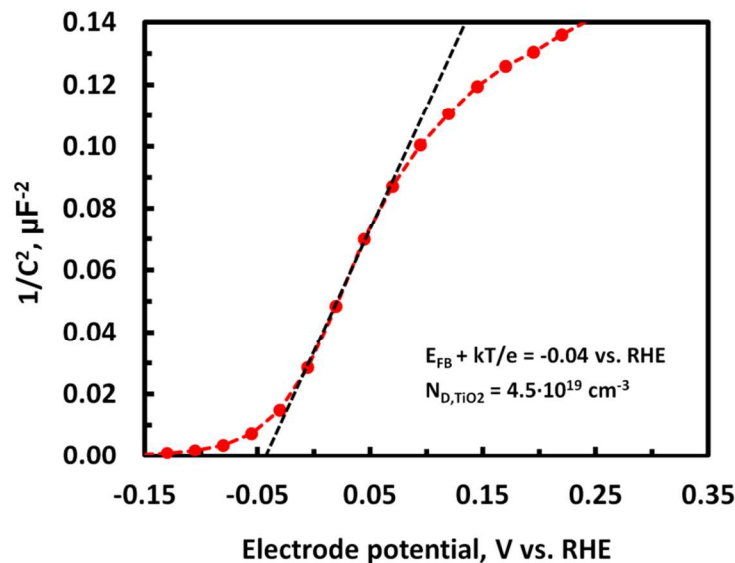


Figure S 4. Mott-Schottky plot of sputtered 100 nm $\text{TiO}_2/5$ nm Ti on n^+ Si surface.

5. Role of p^+ layer

Some samples were fabricated without p^+ doped layer to demonstrate the importance of having a p^+ sheet-conducting layer. The schematic cross sections of these samples can be found in Figure S5. All layers are fabricated using same process as mentioned in table S1. Figure S6 shows the cyclic voltammogram (CV) for photocatalytic H_2 evolution of the pn^+ -Si electrodes with direct back contact at the middle of the sample and back contact on Al charge collector under front side illumination. H_2 could be visually observed bubbling off from the semiconductor/liquid interface as the current increased, and it was confirmed by GC measurement that hydrogen is produced with high Faradaic efficiency (Figure S9 in SI†). Both samples have open circuit voltage (V_{oc}) well in excess the H^+/H_2 redox potential (0 V vs. RHE).

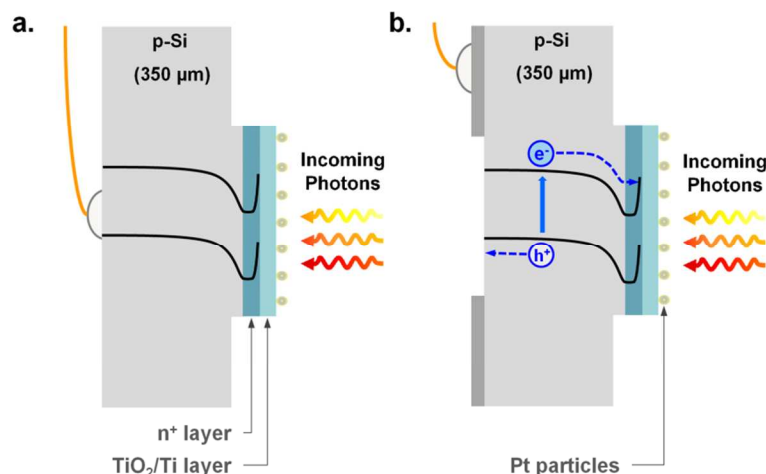


Figure S 5. Schematic cross section of front-illuminated samples of Figure S6. Cu-wire is directly connected on the back side (a) using Ga-In eutectic and Ag paste. Cu-wiring on Al layer (b) is also used to demonstrate the importance of having a sheet-conducting layer. These samples were covered with Teflon tape before the photochemical experiments.

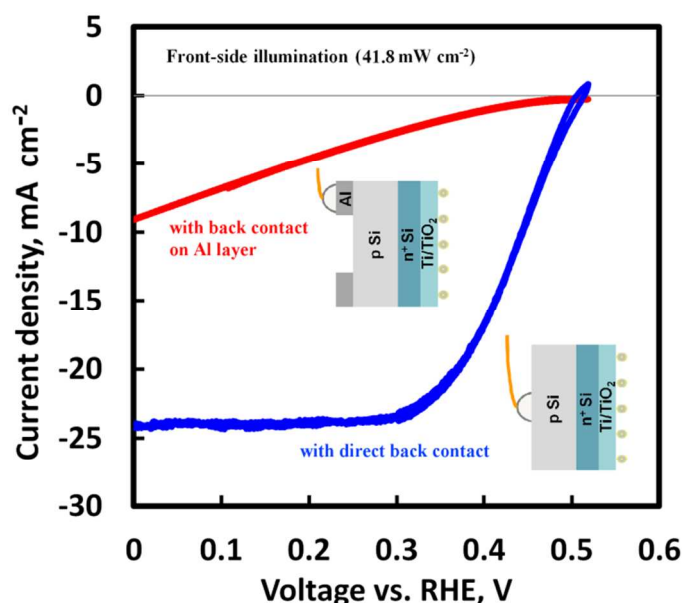


Figure S 6. CV of a pn^+ -Si photocathode with direct back contact (blue) and one with back contact on Al charge collection layer (red) under front-illumination. This illustrates the severe series-resistance problem and thus the need for a transparent interlayer to form an efficient pathway for carriers.

The pn^+ -Si with direct back contact has an onset of 0.49 V vs. RHE with J_L approximately 24 mA cm^{-2} under these conditions. On the other hand, the sample with an Al layer (red curve) back contact has a similar V_{oc} , but it has a very low J_L at 0 V vs. RHE due to a high series resistance. This shows that simply adding a ring-shaped Al charge collector layer is not sufficient to provide an efficient pathway for injected holes from Si. Thus there is a need for an additional transparent layer with low lateral resistance (R_l) in order to transfer the holes to the Al layer without

significant Ohmic loss. Furthermore, since we wish to illuminate from the back, this transport layer must be transparent. This was achieved via a shallow boron doped p^+ layer, which is formed between the Al back contact and the p-Si substrate as shown in Figure 2a and b. This structure makes the overall series resistance of the device comparable to a conventional Si device with direct back contact. It was estimated that a doping concentration of 10^{20} cm^{-3} ($5 \cdot 10^{16} \text{ at/cm}^2$ at 100 keV) of boron could provide a sufficiently low sheet resistance to the Si surface⁹ and consequently an efficient carrier transport pathway.

8. Mathematical derivation of charge collection probability under back-illumination

Let us first consider a semiconductor slab of thickness L , with surface recombination velocity V_s at $z = L$, and diffusivity D for the minority carriers (electrons). We define the normalized surface recombination velocity as $S = V_s/D$. At $z = 0$ the excess electron density n_{e0} is assumed. The excess carrier density in steady state is governed by a continuity equation aforementioned in methods section. The solution of the equation is:

$$n_e = n_{e0} \frac{\cosh \frac{L-z}{L_e} + SL_e \sinh \frac{L-z}{L_e}}{\cosh \frac{L}{L_e} + SL_e \sinh \frac{L}{L_e}}$$

The electron flux density is then:

$$F = -D \nabla n_e = \frac{D}{L_e} n_{e0} \frac{\sinh \frac{L-z}{L_e} + SL_e \cosh \frac{L-z}{L_e}}{\cosh \frac{L}{L_e} + SL_e \sinh \frac{L}{L_e}}$$

Assume now electron hole pair generation at $z = z_0$ in a simple pn-junction model, where the total absorber thickness is L and the depletion layer has the boundaries at $z = z_b$ and $z = z_e$ while the back side at $z = 0$ has normalized recombination rate S . At the junction boundaries $n_{e0} = 0$ is assumed. The minority carrier electrons generated at z_0 will diffuse to the left and right and create the steady state excess carrier profile shown in Fig. S7; only the electron flux density at z_b contributes to the collected electrons. Thus the collection probability $C_p(z)$ is the flux density at z_b divided by the sum of flux density magnitudes at z_0 . The flux densities magnitudes can be written as follows:

$$F(z_b) = \frac{D}{L_e} n_{e,z_0} \frac{1}{\sinh \frac{z_b - z_0}{L_e}}, \quad \text{Note } S \rightarrow \infty \text{ at } z = z_b;$$

$$F(z_0)_{right} = \frac{D}{L_e} n_{e,z_0} \frac{\cosh \frac{z_b - z_0}{L_e}}{\sinh \frac{z_b - z_0}{L_e}};$$

$$F(z_0)_{left} = \frac{D}{L_e} n_{e,z_0} \frac{\sinh \frac{z_0}{L_e} + S L_e \cosh \frac{z_0}{L_e}}{\cosh \frac{z_0}{L_e} + S L_e \sinh \frac{z_0}{L_e}}$$

and thus the collection probability becomes:

$$C_p(z) = \frac{F(z_b)}{F(z_0)_{right} + F(z_0)_{left}} = \frac{1}{\cosh \frac{z_b - z_0}{L_e} + \sinh \frac{z_0}{L_e} \cdot \frac{\sinh \frac{z_0}{L_e} + S L_e \cosh \frac{z_0}{L_e}}{\cosh \frac{z_0}{L_e} + S L_e \sinh \frac{z_0}{L_e}}}$$

In the depletion layer the $C_p(z)$ is 1. As already shown in our previous work³, the depletion layer of our pn^+ Si is approximately 640 nm, but its contribution under the back-illumination is negligibly small since the normalized charge generation rate $G(z)$ is close to zero at the junction boundary.

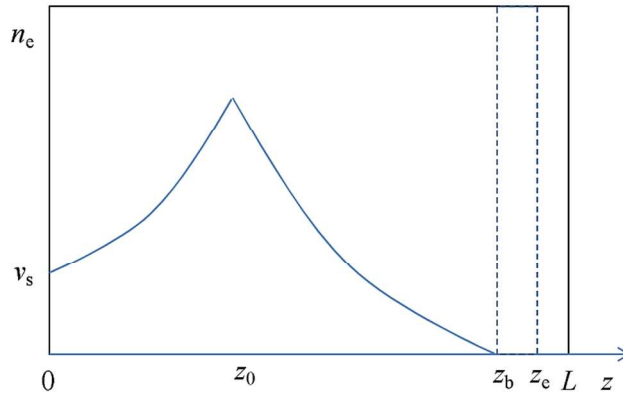


Figure S 7. Simple photoabsorber model with pn-junction. The blue curve illustrates how electron density changes with depth in photoabsorber when the electron-hole pair generation occurs at point z_0 .

6. Absorption properties of silicon

The optical properties of silicon were measured at 300K¹⁰. The absorption length (δ_p) is the inverse of the absorption coefficient (α). The index of refraction (n) for silicon is also plotted.

These n and α were used in this work for determination of absorbance (a) by using Equation 6 in main manuscript.

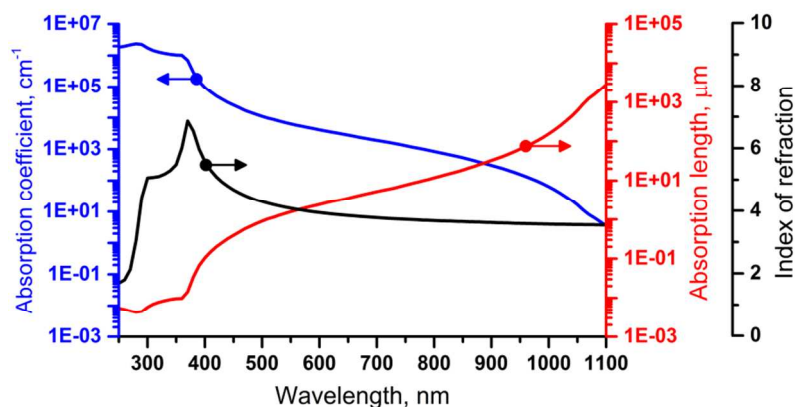


Figure S 8. Absorption coefficient of silicon in cm^{-1} as a function of the wavelength (blue) and absorption length in silicon (red). Silicon is an indirect band gap semiconductor so there is a long tail in absorption out to long wavelengths. The data is graphed on a log scale, and the drop in absorption at the band gap (around 1100 nm) is sharper than might first appear. The n value, *i.e.* index of refraction, of silicon is also plotted (black).

7. H_2 quantification method

H_2 quantification was carried out using a gas chromatograph (Hewlett Packard 5890 Series II) equipped with a Molsieve-5A PLOT column (carrier gas: Ar), a thermal conductivity detector and automated gas sampling. A diaphragm pump (KNF, NF5RPDCB-4) was used to keep the gas in the working electrode compartment flowing through the gas chromatograph (GC) closed sample loop and bubbling through the electrolyte. Before the reactions, both the counter and the working electrode compartments were flushed with Ar gas and the cell was closed off. The headspace gas composition of the working electrode was sampled every 10 minutes throughout the entire length of the experiments (as the red dots in the plot below). A pure Pt wire was used as a standard to calibrate the H_2 signal before the experiment using the same GC. The number of moles of H_2 , n_{H_2} , was then extracted using the ideal gas law. Finally, the corresponding charge, Q_{H_2} , was obtained via the equation $Q_{\text{H}_2} = 2Fn_{\text{H}_2}$, where F is the Faraday constant. In Figure S9, fluctuation of the photocurrent in the first 30 min is shown, and then stabilizes. This might be due to the unstable light irradiation. The evolved H_2 as measured by GC of the head space is represented by red dots. The measured amount of H_2 closely matches the expected amount of H_2 which is calculated taking into account the amount of charge passed through the circuit (black

dashed line). This demonstrates that the current is indeed due to photocatalytic hydrogen evolution close to unity Faraday efficiency.

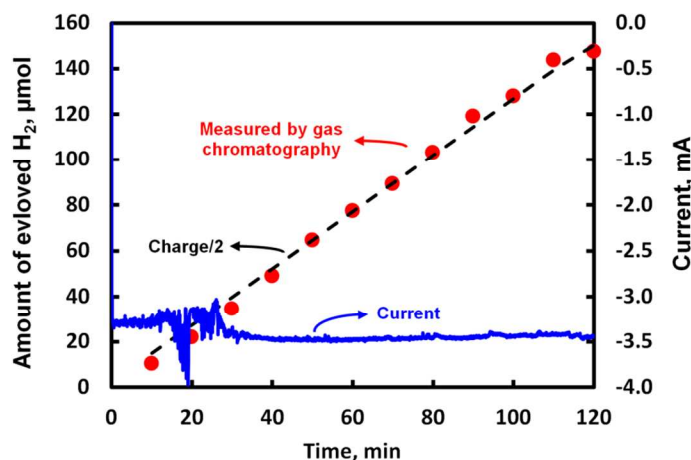


Figure S 9. Hydrogen evolution as a function of time measured with a gas chromatograph and corresponding current over the back-illuminated Pt/TiO₂/Ti/p⁺pn⁺ Si at 0 V vs. RHE. The illuminated area is 0.201 cm² and the sample is under red-light irradiation (Xe lamp with AM 1.5 and 635-nm-cut-off filters). The current initially decays 5% in the first 30 min and then stabilizes.

9. Thickness effect on IPCE

The slopes and intensities of incident photon to current efficiency (IPCE) decrease with the thickness of Si under back illumination. This is highly related with L_e/L decrease effect on the charge collection probability as shown in Figure 7 in main manuscript. On the other hand, IPCE under the front-illumination showed gradual decrease only in long wavelength range with decrease of Si thickness. Since photons with longer wavelengths penetrate deeper into the silicon, under back-illumination electron-hole pairs generated from longer wavelength photons are therefore generated closer to the pn⁺-junction boundary under back-illumination. However, in the front illuminated case most of carriers are generated close to the pn⁺-junction regardless of the Si thickness.

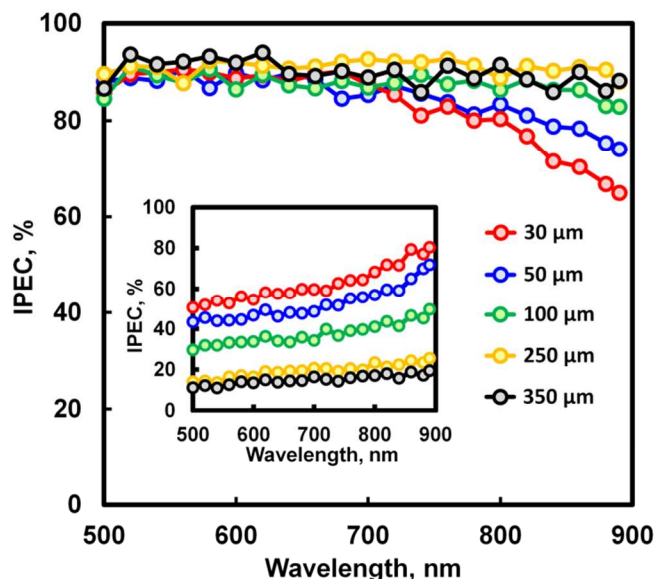


Figure S 10. IPCE from the Si photocathodes with various thicknesses under front and the back-illumination (inset). The slope and intensity of IPCE increase gradually with decrease of Si thickness under the back-illumination, whereas for the front-illuminated case intensity decreases slightly with decrease of the thickness only in the long wavelength range.

10. Reflectance and transmittance measurement

Reflectance from the back side (Quartz/air/SiO₂/Si side) and front side (TiO₂/Ti/Si) was measured by using an integrating sphere (Mikropack ISP-50-8-R-GT). As shown in Figure S11 the reflectance of the back side exceeds 16% over the full spectral range, whereas reflectance from the front side (TiO₂/Ti/Si) was less than 10% at wavelengths ≥ 635 nm. It seems that the high reflectivity of the back side contributed to the low IPCE at longer wavelengths under the back-illumination. Also, the high IPCE over 90% under front-illumination might be due to this anti-reflective property of the TiO₂ protection layer.

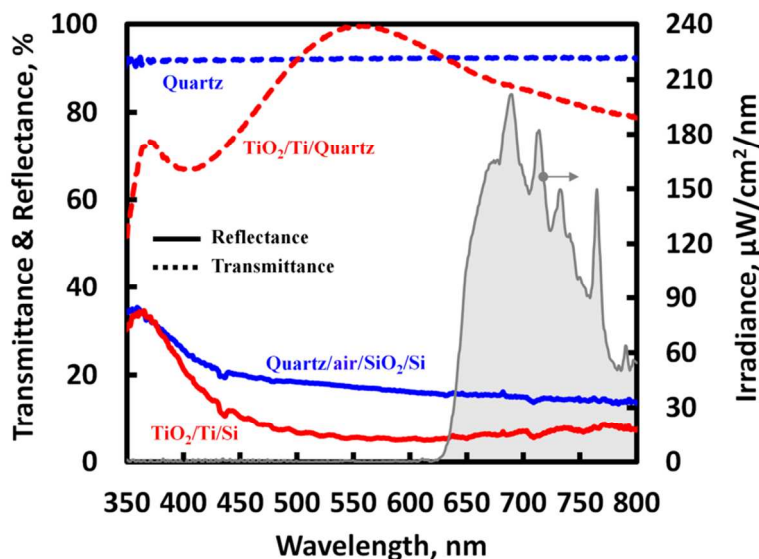


Figure S 11. Reflectance of Quartz/air/SiO₂/Si and TiO₂/Ti/Si are given (solid) with the transmittance of 500- μm -thick Pyrex and 100-nm-thick TiO₂ which are used as a cover glass for the back-side and a protection layer for the front-side, respectively (dot). Irradiance of the light from the solar simulator used in this work is also given.

11. IPCE & APCE vs. $C_p(z)$

The measured IPCE corresponds to incident photon to current efficiency ratio, and it is the ratio of the number of charge carriers collected by the device to the number of photons of a given energy shining on the device from outside (incident photons). To estimate more precise charge collection behavior, we have calculated the absorbed photon to current efficiency ratio (APCE), which is the ratio of the number of charge carriers collected by the device to the number of photons of a given energy that are absorbed by the device. The APCE can be calculated from ICPE by using following relationship:

$$APCE = \frac{IPCE}{1 - R - T}$$

where R is the reflectance and T the transmittance of the sample. The measured reflectance data in Figure S11 were used in this equation. As shown in Figure S12, the APCE in term of absorption depth of the light in Si shows a behavior quite similar to calculated $C_p(z)$ with $L_e = 400 \mu\text{m}$ and $S = 170 \text{ cm}^{-1}$. (Note: for APCE the transmittance of the Si wafer was not taken into account).

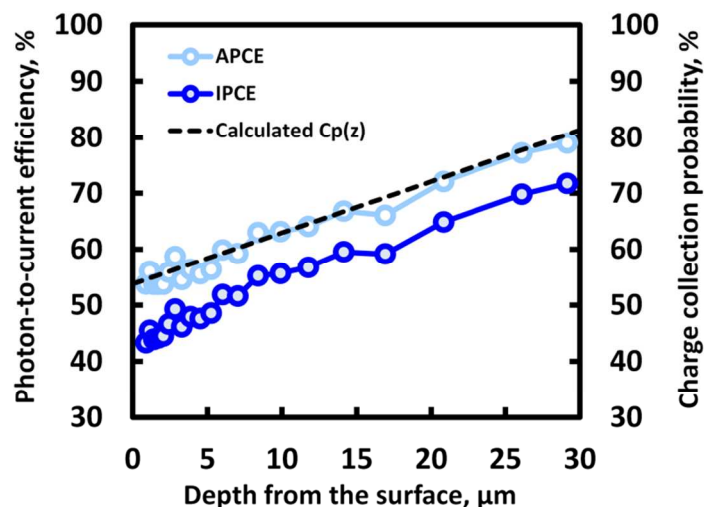


Figure S 12. Incident photon to current efficiency (IPCE, dark blue) and Absorbed photon to current efficiency (APCE, light blue), which was converted from IPCE considering the reflectance of back side. Calculated $C_p(z)$ is also shown to compare with APCE.

12. Thickness effect on CV under back-illumination

Photocurrent of Si photocathode increases under back-illumination along with the decrease of the thickness. 50- μm -thick Sample showed highest current density over 17 mA cm^{-2} . However 30- μm -thick sample is outperformed by the 50- μm -thick sample indicating that absorption losses at long wavelength start to dominate the charge collection losses.

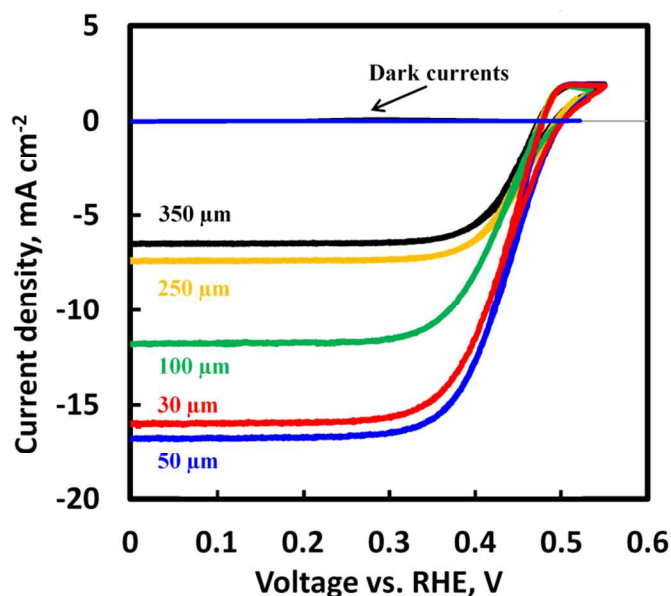


Figure S 13. CVs of Si photocathodes with various thicknesses. The total irradiance is 41.8 mW cm^{-2} . Assuming that S and L_e of all samples is same, this shows how L_e/L affects J_L of the device.

1. B. Seger, T. Pedersen, A. B. Laursen, P. C. K. Vesborg, O. Hansen, I. Chorkendorff, *Using TiO₂ as a conductive protective layer for photocathodic H₂ evolution*, J. Am. Chem. Soc., 2013, **135**, 1057–1064.
2. L. Vivien, L. Pavesi, *Handbook of silicon photonics*, Taylor & Francis, Boca Raton, 2013, ch. 1.3., p. 26.
3. The NIST reference on constants, units, and uncertainty, <http://physics.nist.gov/cgi-bin/cuu/Value?ep0> (accessed Nov. 24, 2014).
4. M.-K. Lee, H.-C. Lee, C.-M. Hsu, *High dielectric constant titanium oxide grown on amorphous silicon by metal-organic chemical vapour deposition*, *Semicond. Sci. Technol.*, 2006, **21**, 604-607.
5. H. P. R. Frederikse, CRC Handbook of Chemistry and physics, ed. by D. R. Lide, 78th edition, 1997, pp 12.
6. N. Dasgupta, A. Dasgupta, *Semiconductor devices: modeling and technology*, Prentice-Hall, New Delhi, 2004, ch. 1.3.10., pp. 30.
7. D. M. King, X. Du, A. S. Cavanagh, A. Weimer, *Confinement in amorphous TiO₂ films studied using atomic layer deposition*, *Nanotechnology*, 2008, **19**, 445401-445406.
8. J. Bisquert, A. Zaban, M. Greenshtein, I. Mora-Sero, *Determination of rate constants for charge transfer and the distribution of semiconductor and electrolyte electronic energy levels in dye-sensitized solar cells by open-circuit photovoltage decay method*, J. Am. Chem. Soc., 2004, **126**, 13550-13559.
9. W. R. Thurber, R. L. Mattis, Y. M. Liu, J. J. Filliben, *Resistivity-dopant density relationship for boron-doped silicon*, J. Electrochem. Soc., 1980, **127**, 2291-2294.
10. M. A. Green, M. J. Keevers, *Optical properties of intrinsic silicon at 300 K*, Prog. Photovoltaics, 1995, **3**, 189-192.